Soil Moisture Retrieval in Agricultural Fields Using Adaptive Model-Based Polarimetric Decomposition of SAR Data

Lian He, Rocco Panciera, *Member, IEEE*, Mihai A. Tanase, *Member, IEEE*, Jeffrey P. Walker, *Member, IEEE*, and Qiming Qin

***Abstract*—The aim of this paper was to estimate soil moisture in agricultural crop fields from fully polarimetric L-band synthetic aperture radar (SAR) data through the polarimetric decomposition of the SAR coherency matrix. A nonnegative-eigenvalue-decomposition scheme, together with an adaptive volume scattering model, is extended to an adaptive model-based decomposition (MBD) (Adaptive MBD) model for soil moisture retrieval. The Adaptive MBD can ensure nonnegative decomposed scattering components and allows two parameters (i.e., the mean orientation angle and a degree of randomness) to be determined to characterize the volume scattering. Its performance was tested using airborne SAR data and coincident ground measurements collected over agricultural fields in southeastern Australia and compared with previous MBD methods (i.e., the Freeman three-component decomposition using the extended Bragg model, the Yamaguchi three-component decomposition, and an iterative generalized hybrid decomposition). The results obtained with the newly proposed decomposition scheme agreed well with expectations based on observed plant structure and biomass levels. The new method was superior in tracking soil moisture dynamics with respect to previous decomposition methods in our study area, with root-mean-square error of soil moisture estimations being 0.10 and 0.14 m^3/m^3, respectively, for surface and double-bounce components. However, large variability in the achieved soil moisture accuracy was observed, depending on the presence of row structures in the underlying soil surface.**

***Index Terms*—Agricultural fields, polarimetric decomposition, synthetic aperture radar (SAR) polarimetry, soil moisture.**

Manuscript received June 4, 2015; revised January 25, 2016; accepted March 1, 2016. Date of publication April 5, 2016; date of current version June 1, 2016. This work was supported in part by the National Natural Science Foundation of China under Grants 41230747 and 41401375, by a scholarship from the China Scholarship Council, and by the Australian Research Council under Grants DP0984586, LE0882509, and FS100100040. *(Corresponding author: Rocco Panciera.)*

L. He is with the Institution of Remote Sensing and GIS, Peking University, Beijing 100871, China, and also with the Department of Civil Engineering, Monash University, Melbourne, Vic. 3800, Australia (e-mail: helian_2006@126.com).

R. Panciera is with the Department of Civil Engineering, Monash University, Melbourne, Vic. 3800, Australia, and also with the Cooperative Research Centre for Spatial Information, University of Melbourne, Melbourne, Vic. 3053, Australia (e-mail: pancerarocco@gmail.com).

M. A. Tanase is with the Cooperative Research Centre for Spatial Information, University of Melbourne, Melbourne, Vic. 3053, Australia (e-mail: mihai76@gmail.com).

J. P. Walker is with the Department of Civil Engineering, Monash University, Melbourne, Vic. 3800, Australia (e-mail: jeff.walker@monash.edu).

Q. Qin is with the Institution of Remote Sensing and GIS, Peking University, Beijing 100871, China (e-mail: qmqin@pku.edu.cn).

Color versions of one or more of the figures in this paper are available online at http://ieeexplore.ieee.org.

Digital Object Identifier 10.1109/TGRS.2016.2542214

I. Introduction

POLARIMETRIC synthetic aperture radar (SAR) is a promising remote sensing technique for soil moisture monitoring. The SAR signal is known to contain information about the properties of scatterers, not only on surface characteristics such as soil moisture and surface roughness [1]–[7] but also on the structure and properties of the vegetation canopy [8]–[12]. Moreover, current spaceborne SAR technology allows the fine spatial resolution (from meters to tens of meters) and frequent revisit (from days to weeks) that are needed for soil moisture information to have an impact on agricultural management and hydrological predictions [13].

The SAR backscattered signal from vegetated areas is influenced by vegetation cover and soil surface characteristics such as soil moisture and surface roughness [14]. Soil moisture retrieval from SAR systems having limited viewing capabilities (i.e., single channel, frequency, and incidence angle) is therefore an underdetermined problem [15], [16], due to the lack of sufficient observations for estimating several unknown parameters (i.e., soil moisture, surface roughness, and vegetation elements). Consequently, *a priori* information or assumptions concerning the characteristics of the vegetation layer are required to reduce the number of unknowns and successfully invert radar backscatter models to estimate soil moisture. Such *a priori* information or assumptions are generally in the form of site-specific or vegetation-specific parameters (such as vegetation height, phenology, structure, etc.) in empirical and semiempirical models [17], [18] or, alternatively, highly detailed information on vegetation parameters for numerical and theoretical models [19], [20], which are laborious to collect in the field. Alternatively, *a priori* assumptions have to be made on the value, range, or probability distribution of one or more of the underlying surface characteristic, as in change-detection methods [21], [22] or statistical probability methods [23], [24]. Multiple-configuration SAR (i.e., concurrent observations at multiple angles and frequencies) is an efficient way to increase the number of SAR observables to solve for soil moisture [25], [26]. Nevertheless, routine time series of multiple-configuration SAR observations having the high temporal frequency required for tracking soil moisture changes are still difficult to obtain.

The availability of missions with fully polarimetric SAR capabilities such as RADARSAT-2 and ALOS PALSAR-1/2 has increased the interest in methods that exploit polarimetric radar information in order to completely characterize the target characteristics [27]–[30]. Fully polarimetric SAR systems provide, for each pixel, the full complex scattering matrix, including amplitude and phase information of the four transmit–receive channels (HH, HV, VH, and VV). This contains a wealth of information on the target properties, particularly vegetation properties such as size, shape, orientation, and dielectric constant of leaves, stalks, and fruit [11], [31]. Therefore, in the context of soil moisture retrieval, fully polarimetric SAR observations hold tremendous potential for quantifying and removing the impact of vegetation on the backscattered signal without (or with limited use of) *a priori* assumptions and information on the vegetation structure [26], [32]–[35].

Among the many methods proposed in past decades for exploiting the information contained in fully polarimetric SAR data, there are two main approaches: the eigenvalue-based decomposition approaches and the model-based decomposition (MBD) approaches, pioneered by Cloude and Pottier [28] and Freeman and Durden [29], respectively. Both methods decompose the measured complex scattering matrix into a combination of a few simple components and therefore are referred to as polarimetric decomposition methods. These components are then linked to physical scattering mechanisms. The polarimetric decomposition techniques have shown potential for application to soil moisture retrieval in agricultural areas. The eigenvalue-based decomposition method has been used for soil moisture retrieval through the (extended) Bragg model [3] or the polarimetric two-scale model (PTSM) [6]. However, these methods could not separate the individual contributions of the surface and vegetation layers to the scattering matrix and therefore have limited applicability in the presence of agricultural crops. A more promising attempt to retrieve soil moisture under crop canopies was that of Hajnsek *et al.* [32] by using a variety of modified model-based polarimetric decompositions within the framework of the Freeman–Durden MBD (Freeman MBD) in [29]. Although results indicated the ability to classify soil moisture into three to five different moisture classes for each crop type, low spatial inversion rates (the relative amount of pixels in the image that can be successfully inverted) were observed, and therefore, these methods could not provide spatially continuous soil moisture maps. Meanwhile, these methods were confined to simple volume scattering models. To overcome these limitations, an iterative generalized hybrid MBD (referred to as the Hybrid MBD) was proposed in [35] by combining model-based and eigenvalue-based techniques together with a generalized volume scattering model. The Hybrid MBD demonstrated a major step forward by achieving high inversion rates for a variety of vegetation covers. However, the contribution of the double-bounce component in the Hybrid MBD had to be neglected in order to achieve a physically constrained solution for the vegetation volume intensity. In the proposed polarimetric decomposition methods in [32] and [35], scattering reflection symmetry was assumed (i.e., $\langle S_{\rm hh}S_{\rm hv}^*\rangle = \langle S_{\rm vv}S_{\rm hv}^*\rangle = 0$) to determine the volume contribution. Additionally, some MBDs [32] could not ensure nonnegative decomposed powers due to the overestimation of volume scattering [36], [37].

As an alternative to the previous approaches, an adaptive volume model (Adaptive VM) was recently proposed in [38], which does not require the assumption of scattering reflection symmetry when determining the volume contribution. The Adaptive VM allows for the variable orientation angle and degree of randomness of the vegetation scattering elements to be determined without any *a priori* assumptions. Based upon the adaptive volume scattering model, an Adaptive MBD scheme was proposed in [27], which could ensure that all the decomposed components have nonnegative powers. Hence, the two deficiencies (i.e., limited volume scattering model and negative decomposed powers) faced by the previous approaches could be avoided in the Adaptive MBD. To our knowledge, the advanced polarimetric analysis techniques proposed in [27] and [38] have not yet been tested for soil moisture retrieval in an agricultural setting. However, this advanced polarimetric decomposition approach was not designed for soil moisture inversion since the Adaptive MBD does not account for the fact that the ground components must be inverted using physically based models. This paper shows how the Adaptive MBD model is extended to a novel soil moisture inversion scheme. The objective of this paper is therefore to assess the advantage in soil moisture estimation from using a more realistic modeling of the vegetation layer. This is tested by applying the Adaptive MBD to airborne SAR and field data and its performance compared against the previous MBD approaches in [32] and [35].

This paper is organized as follows. Section II provides a detailed theoretical description of the Adaptive MBD tested. Section III briefly describes the airborne and ground data sets. Results and discussion on the comparison between Adaptive MBD and previous MBD methods, the evaluation of different volume models, and the soil moisture retrieval are then presented in Section IV, followed by conclusions in Section V.

II. Methods

A. Framework of NNED

In model-based polarimetric decomposition, the measured coherency (or covariance) matrix of vegetated areas is usually expanded by a linear combination of several individual matrices, which are then interpreted according to their scattering mechanisms. The well-known MBDs include a three-component MBD proposed by Freeman and Durden [29] and a four-component MBD proposed by Yamaguchi *et al.* [39]. One of the problems associated with the MBDs is that the powers of surface and double-bounce scattering components may become negative due to the overestimation of volume scattering power [30], [36] and [37]. However, as pointed out by Van Zyl *et al.* [36], each decomposed scattering component represents a physical scattering process and therefore should never be negative. To account for this property, a nonnegative eigenvalue decomposition (NNED) model was proposed in [30]. In the NNED, the measured coherency matrix $\mathbf{T_{data}}$ is decomposed into surface scattering $\mathbf{T_s}$, double-bounce scattering $\mathbf{T_d}$, and volume scattering $\mathbf{T_v}$ components. The general form is [30]

$$\begin{bmatrix} T_{11} & T_{12} & T_{13} \\ T_{12}^* & T_{22} & T_{23} \\ T_{13}^* & T_{23}^* & T_{33} \end{bmatrix} = [\mathbf{T_{data}}] = f_v[\mathbf{T_v}] + f_s[\mathbf{T_s}] + f_d[\mathbf{T_d}] + [\mathbf{T_{residual}}] \quad (1)$$

where the superscript $*$ denotes complex conjugation; f_{v}, f_{s}, and f_{d} are the scattering intensities for volume, surface, and double-bounce scattering components, respectively; and $\mathbf{T_{residual}}$ is the residual component after the volume, surface, and double-bounce components have been subtracted.

After subtracting the volume component $\mathbf{T_v}$ from the observed coherency matrix $\mathbf{T_{data}}$, the remainder coherency matrix $\mathbf{T_{remainder}}$ can be generally written as

$$[\mathbf{T_{remainder}}] = [\mathbf{T_{data}}] - f_v \begin{bmatrix} V_{11} & V_{12} & V_{13} \\ V_{12}^* & V_{22} & V_{23} \\ V_{13}^* & V_{23}^* & V_{33} \end{bmatrix} \tag{2}$$

where $V_{i,j}$ are elements for the volume scattering model.

It should be noted that no specific volume scattering model is assumed in (2) and any physically realizable volume scattering model can be used in the aforementioned equation. To find the volume scattering intensity f_v, a nonnegative eigenvalue approach is utilized, in which the largest value of f_v that ensures that all three eigenvalues of the matrix $\mathbf{T_{remainder}}$ would be greater than or equal to zero is selected in the decomposition. Van Zyl *et al.* [30], [36] analytically derived the formula of f_v by using the eigenvalues of $\mathbf{T_{remainder}}$ when the scattering reflection symmetry holds. When no reflection symmetry is assumed, the characteristic equation of the remainder matrix would be a general cubic polynomial, and the maximum f_v can be achieved by solve a cubic equation in f_v [40]. The maximum f_v can be also numerically calculated by varying f_v to find the maximum f_v in which all three eigenvalues of $\mathbf{T_{remainder}}$ are nonnegative [27]. In this way, the volume scattering power can be determined for a specific volume scattering model.

The remainder $\mathbf{T_{remainder}}$ can be considered as a sum of surface $\mathbf{T_s}$, double-bounce $\mathbf{T_d}$, and residual $\mathbf{T_{residual}}$ components and can be written as

$$[\mathbf{T_{remainder}}] = f_s[\mathbf{T_s}] = f_d[\mathbf{T_d}] + [\mathbf{T_{residual}}]. \tag{3}$$

To estimate the surface $\mathbf{T_s}$, double-bounce $\mathbf{T_d}$, and residual $\mathbf{T_{residual}}$ components, the ground components are assumed to satisfy the reflection symmetry assumption, and the eigenvalue decomposition is applied [30], [41], with the three individual components being

$$[\mathbf{T_s}] = \begin{bmatrix} \cos^2\alpha_s & \cos\alpha_s \sin\alpha_s e^{i\phi_s} & 0 \\ \cos\alpha_s \sin\alpha_s e^{-i\phi_s} & \sin^2\alpha_s & 0 \\ 0 & 0 & 0 \end{bmatrix} \tag{4a}$$

$$[\mathbf{T_d}] = \begin{bmatrix} \cos^2\alpha_d & \cos\alpha_d \sin\alpha_d e^{i\phi_d} & 0 \\ \cos\alpha_d \sin\alpha_d e^{-i\phi_d} & \sin^2\alpha_d & 0 \\ 0 & 0 & 0 \end{bmatrix} \tag{4b}$$

$$[\mathbf{T_{residual}}] = f_{\mathrm{sd}} \begin{bmatrix} 0 & 0 & 0 \\ 0 & 0 & 0 \\ 0 & 0 & 1 \end{bmatrix} \tag{4c}$$

where f_{sd} is the scattering intensity for the residual component, α_s and α_d are the scattering angles characterizing the surface and double-bounce scattering mechanisms, and ϕ_s and ϕ_d are the scattering phases for surface scattering and double-bounce scattering, respectively. Generally, the surface scattering angle α_s ranges between 0° and 45°, while the double-bounce scattering angle α_d locates in the range of 45°–90°. It should be pointed out that, in the eigenvalue decomposition, the surface component $\mathbf{T_s}$ and the double-bounce component $\mathbf{T_d}$ are assumed to be orthogonal. The orthogonality condition can be written as [37], [42]

$$\alpha_s + \alpha_d = \frac{\pi}{s} \text{ and } \phi_s + \phi_d = \pm\pi. \tag{5}$$

The matrix $\mathbf{T_{residual}}$ in (3) is the residual power after subtracting the volume, surface, and double-bounce components. In general, the residual component will contain additional cross-polarized power (in the T_{33} element of $\mathbf{T_{residual}}$) that could represent terrain effects and rough surface scattering [30].

B. Adaptive MBD Model

The vegetation canopy is often approximated as a cloud of equally shaped particles. Under this approximation, several volume scattering models have been proposed under the reflection symmetry condition by considering the effects of the orientation and the shape of volume particles [29], [35], [39], [43] and [44]. A promising general model, which requires no scattering reflection symmetry assumption, was introduced by Arii *et al.* [38]. This generalized volume model describes the vegetation canopy as a cloud of thin cylinders characterized by two parameters: the mean orientation angle of the dipoles and the degree of randomness around that mean orientation angle. In the form of the coherency matrix, this volume model can be expressed as [38]

$$\mathbf{T_v}(\theta_0, \sigma) = \mathbf{T}_{\boldsymbol{\alpha}} + p(\sigma)\mathbf{T}_{\boldsymbol{\beta}}(\theta_0) + q(\sigma)\mathbf{T}_{\boldsymbol{\gamma}}(\theta_0) \tag{6}$$

with

$$\mathbf{T}_{\boldsymbol{\alpha}} = \frac{1}{4}\begin{bmatrix} 2 & 0 & 0 \\ 0 & 1 & 0 \\ 0 & 0 & 1 \end{bmatrix} \tag{7a}$$

$$\mathbf{T}_{\boldsymbol{\beta}}(\theta_0) = \frac{1}{4}\begin{bmatrix} 0 & -\cos(2\theta_0) & \sin(2\theta_0) \\ -\cos(2\theta_0) & 0 & 0 \\ \sin(2\theta_0) & 0 & 0 \end{bmatrix} \tag{7b}$$

$$\mathbf{T}_{\boldsymbol{\gamma}}(\theta_0) = \frac{1}{4}\begin{bmatrix} 0 & 0 & 0 \\ 0 & \cos(4\theta_0) & -\sin(4\theta_0) \\ 0 & -\sin(4\theta_0) & -\cos(4\theta_0) \end{bmatrix} \tag{7c}$$

where θ_0 is the mean orientation angle and σ is the degree of randomness. The coefficients $p(\sigma)$ and $q(\sigma)$ are characterized by sixth-order polynomials in terms of σ as in [27]. The parameter σ ranges from 0 to 0.91. There are two extreme cases: the uniform distribution with $\sigma = 0.91$ when the thin cylinders are uniformly randomly distributed and the delta distribution with $\sigma = 0$ when all the individual cylinders have consistent orientation.

For the general case of volume scattering model in (6), the reflection symmetry is not guaranteed except for specific mean orientation angles. This generalized model allows for a variable orientation angle and randomness and is therefore referred to in this paper as the "Adaptive VM."

Based on the Adaptive VM, the NNED of (1) was extended to an Adaptive MBD [27] by replacing the volume component in (1) with (6). To find the best fit decomposition, the power in the residual matrix is evaluated for all pairs of randomness and mean orientation angles, and the parameter set that minimizes the power associated with the residual matrix will be selected.

C. Modifications of the Adaptive MBD

The Adaptive MBD was not designed for soil moisture inversion since it does not account for the fact that ground components must be physically invertible. This section shows how the Adaptive MBD can be extended to a novel soil moisture inversion scheme.

In the Adaptive MBD [27], there is no need to determine the dominant scattering component since the ground components are separated by the eigenvalue decomposition. However, for soil moisture inversion, the inverted scattering component must be dominant as shown in [32]. Therefore, before applying the Adaptive MBD, the scattering dominance is first determined. To determine the dominance between surface and double-bounce scattering mechanisms, the sign of $\mathrm{Re}(S_{\mathrm{hh}}S_{\mathrm{vv}}^*)$ after the removal of the volume contribution using a random volume is utilized [29], [32]. Surface scattering is dominant if the term $\mathrm{Re}(S_{\mathrm{hh}}S_{\mathrm{vv}}^*)$ is positive; otherwise, double-bounce scattering is dominant.

The surface scattering component $\mathbf{T_s}$ is usually modeled by the (extended) Bragg model [3], [32], [45] or the PTSM [6], [7]. The original Bragg model [45] does not account for depolarization effects and is not able to describe cross-polarized scattering. In the extended Bragg (X-Bragg) model [3], [32] and the PTSM [6], [7], the cross-polarization returns were induced through a line-of-sight rotation of the surface coherency matrix since terrain slopes in the azimuth direction could rotate the polarization basis of the scattering matrix. The azimuthal slope variations are more likely related to large-scale surface roughness (i.e., a few tens of centimeters, but less than a SAR resolution cell), and therefore, these two models are more suitable for scattering surface composed of rough randomly tilted facets (large with respect to the radar wavelength, but small with respect to the sensor resolution) [6], [7]. However, the use of the X-Bragg or the PTSM will increase the number of unknown parameters, which has to be fixed by setting empirical additional constraints [32], [46]. In this paper, no analytical form is assumed for the surface scattering component, which is considered as the sum of $\mathbf{T_s}$ and $\mathbf{T_{residual}}$ in (3) as

$$[\mathbf{T_{surface}}] = f_s[\mathbf{T_s}] + [\mathbf{T_{residual}}]. \tag{8}$$

The normalized correlation coefficient of $\mathbf{T_{surface}}$ is one

$$\gamma_{(\mathrm{hh+vv})(\mathrm{hh-vv})} = \frac{\langle (S_{\mathrm{hh}} + S_{\mathrm{vv}})(S_{\mathrm{hh}} - S_{\mathrm{vv}})^* \rangle}{\sqrt{\langle |S_{\mathrm{hh}} + S_{\mathrm{vv}}|^2 \rangle \langle |S_{\mathrm{hh}} - S_{\mathrm{vv}}|^2 \rangle}} = 1. \tag{9}$$

As a consequence, the surface scattering model in (8) does not account for depolarization effects [3]. The cross-polarization term of $\mathbf{T_{surface}}$ is assumed mainly due to the rough surface scattering [47] associated with small-scale surface roughness (a few centimeters, comparable with the radar wavelength).

For soil moisture inversion, the copolarization ratio p and cross-polarization ratio q are first reconstructed from the decomposed coherency matrix of the surface component (i.e., $f_s * \mathbf{T_s} + \mathbf{T_{residual}}$), with soil moisture and surface roughness consequently obtained by inverting the empirical Oh surface scattering model [48]. The decomposed surface component is attenuated by extinction through the volume [37], [49] and hence is not the same as the bare surface return. Therefore, the polarization ratios p and q in the Oh model are biased due to differential extinction, i.e., the difference between extinction at V and H polarizations. However, under the assumption that the extinction coefficients from different polarizations are equal, the polarization ratios p and q are preserved. This is the main advantage of the utilization of the Oh model since it employs ratios rather than absolute values for soil moisture retrieval.

The double-bounce component is modeled as a Fresnel reflection between the soil surface and the vertical trunk of a plant with the scattering intensity f_d and scattering mechanism α_d given by [35]

$$\alpha_d = \mathrm{atan}\left(\frac{1}{\alpha_F}\right) \qquad f_d = \frac{f_F}{\sin^2(\alpha_d)} \tag{10}$$

with

$$\begin{aligned} f_F &= \frac{m_d^2}{2}|R_{\mathrm{sh}}R_{\mathrm{th}} + R_{\mathrm{sv}}R_{\mathrm{tv}}e^{i\varphi}|^2 \\ \alpha_F &= \frac{R_{\mathrm{sh}}R_{\mathrm{th}} - R_{\mathrm{sv}}R_{\mathrm{tv}}e^{i\varphi}}{R_{\mathrm{sh}}R_{\mathrm{th}} + R_{\mathrm{sv}}R_{\mathrm{tv}}e^{i\varphi}} \end{aligned} \tag{11}$$

where m_d is the loss factor and φ is the polarimetric phase difference introduced by the vegetation layer. R_{sh}, R_{sv}, R_{th}, and R_{tv} are the Fresnel scattering coefficients of the underlying soil surface and the vegetation trunk plane [32]. The Fresnel scattering coefficients depend on the radar incidence angle θ, the dielectric constant of the soil surface ε_s, and the trunk ε_t. The dielectric constant of the surface ε_s and the trunk ε_t can be retrieved using f_F and α_F as described in detail in [32] in case of the dominant double-bounce component.

To account for the vegetation/roughness attenuation, the loss factor m_d of (11) is assumed as [34]

$$m_d = \exp\left(-\frac{\sin^2(\theta)}{2(\mu_{\max} - \mu_{\min})}\right) \tag{12}$$

with

$$\mu_{\max} = \frac{\lambda_1}{f_v} \qquad \mu_{\min} = \frac{\lambda_2}{f_v} \tag{13}$$

where $\mu_{\max}$ and $\mu_{\min}$ represent the maximum and minimum ground-to-volume ratios defined in [26] and [34], in which λ_1 and λ_2 are eigenvalues of the summed ground component matrix after the removal of the volume component and f_v is the volume intensity obtained by (2). The mean attenuation loss m_d was empirically derived from SAR data over various crop types (i.e., corn, grass, wheat, barley, and rape) [34], and it does not incorporate differential extinction between H polarization and V polarization for randomly oriented volume [26].

To find the best fit decomposition, the Adaptive MBD of (1) is calculated by varying randomness σ and mean orientation angle θ_0 for their entire ranges. The pair of randomness σ and mean orientation angle θ_0 that minimizes the power associated with the residual matrix $\mathbf{T_{residual}}$ is considered as the best fit parameter set. This optimization criterion may underestimate the surface scattering in the case of dominant surface scattering since the residual component is treated as an additional part of the surface component in this paper. Therefore, alternative optimization criteria are utilized to find the best fit parameter by using *a priori* information obtained from the conventional eigenvalue-based decomposition [28]. The surface scattering alpha angle $\alpha_{\min}$ (i.e., the minimum of the three scattering alpha angles) is first calculated from the conventional eigenvalue-based decomposition of $\mathbf{T_{data}}$. Next, the modeled maximum surface scattering angle α_{Bmax} can be obtained from the Bragg model by setting the soil dielectric constant to 40 (the maximum possible soil dielectric constant value assumed in vegetated soils). When surface scattering is dominant and the value of $\alpha_{\min}$ is lower than that of α_{Bmax}, the pair of θ_0 and σ that minimizes $|\alpha_{\min} - \alpha_s|$ is selected, where the α_s is the surface scattering angle obtained from the eigenvalue decomposition of the remainder coherency matrix of (3). When double-bounce scattering is dominant or the value of $\alpha_{\min}$ is greater than that of α_{Bmax}, the power in the residual component is expected to be zero since the double-bounce scattering is assumed to generate no cross-polarization signal. In such case, the pair of θ_0 and σ that minimizes the power in the residual component $\mathbf{T_{residual}}$ is selected.

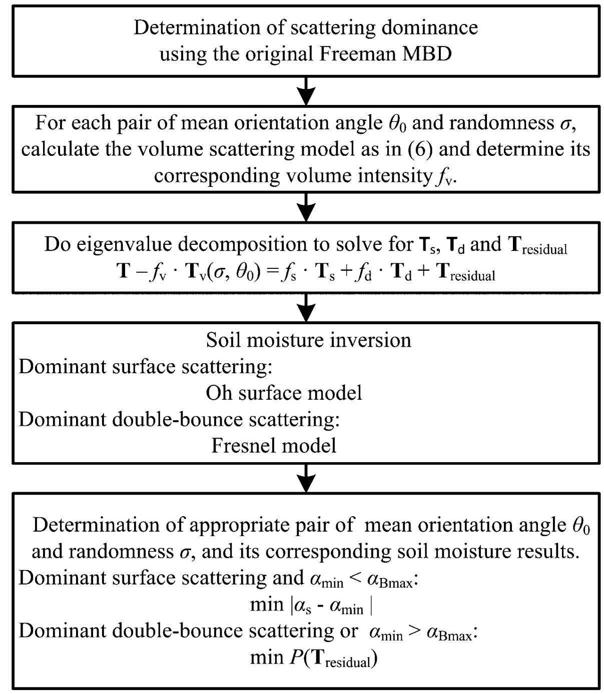

Fig. 1. Adaptive MBD and soil moisture inversion for single pixel.

D. Soil Moisture Inversion by Adaptive MBD

By applying the modifications, the adaptive NNED proposed in [27] is extended to a novel soil moisture inversion scheme, which follows the following steps as also summarized in Fig. 1.

1) Determine the scattering dominance according to the sign of $\mathrm{Re}(S_{\mathrm{hh}} S_{\mathrm{vv}}^*)$ after the removal of the volume component using the Freeman MBD [29].
2) For each pair of σ and θ_0, calculate the volume scattering model as in (6), as well as its corresponding maximum volume intensity f_v. In order to keep simplicity but without loss of generality, a range of discretized values of randomness σ and mean orientation angle θ_0 are used, with the randomness being discrete between 0 and 0.91 (interval steps of 0.03) and the mean orientation angle between 0 and 180° (interval steps of 5°).
3) The eigenvalue decomposition under the assumption of reflection symmetry proposed in [41] is applied to the remainder coherency matrix of (3), with the surface $\mathbf{T_s}$, double-bounce $\mathbf{T_d}$, and residual $\mathbf{T_{residual}}$ components estimated accordingly. The scattering angles α_s and α_d for surface and double-bounce components can also be obtained at the same time.
4) Having decomposed the coherency matrix into surface, double-bounce, and volume components, soil moisture is retrieved from either the surface component or double-bounce component, depending on the scattering dominance. If the surface scattering is dominant, soil moisture is retrieved from the surface component (i.e., $f_s * \mathbf{T_s} + \mathbf{T_{residual}}$) by using the empirical Oh surface scattering model [48]. If the double-bounce component is dominant, soil moisture is retrieved from the Fresnel model of f_F and α_F as detailed in [32]. To obtain physically correct ground scattering components, only the pair of θ_0 and σ that ensures HH $>$ VV for the double-bounce component and HH $<$ VV for the surface component is selected as the candidate of the best fit parameter set.
5) The steps of 2), 3), and 4) are repeated for all pairs of randomness and mean orientation angle. To find the appropriate pair of randomness σ and mean orientation angle θ_0 for each pixel, different optimization criteria are utilized depending on the scattering dominance. If the sign of $\mathrm{Re}(S_{\mathrm{hh}} S_{\mathrm{vv}}^*)$ is positive and the scattering angle $\alpha_{\min}$ from conventional eigenvalue-based decomposition is lower than the maximum surface scattering angle α_{Bmax} from the Bragg model, the pair of θ_0 and σ that minimizes $|\alpha_{\min} - \alpha_s|$ is selected. Otherwise, if the sign of $\mathrm{Re}(S_{\mathrm{hh}} S_{\mathrm{vv}}^*)$ is negative or $\alpha_{\min}$ is greater than α_{Bmax}, the pair of θ_0 and σ that minimizes the power in the residual matrix $P(\mathbf{T}_{\mathrm{residual}})$ (calculated as the matrix trace of $\mathbf{T_{residual}}$) is chosen.

In summary, the adaptive NNED proposed in [27] is extended and incorporated into a novel soil moisture inversion scheme. In this novel scheme, an adaptive volume scattering model without a reflection symmetry assumption is applied, while the surface scattering and double-bounce scattering models are still considered under reflection symmetry. The proposed inversion

TABLE I
POLARIMETRIC DECOMPOSITION MODELS TESTED IN THIS PAPER

Polarimetric Decomposition Models	Surface Scattering Model	Double-Bounce Scattering Model	Volume Scattering Model	Determination of Volume Intensity
Freeman MBD using X-Bragg	X-Bragg model	Fresnel model	Random volume model	Directly derived
Yamaguchi MBD	Bragg model	Fresnel model	Yamaguchi volume model	Directly derived
Hybrid MBD	Bragg model	Fresnel model	Generalized volume model	Physically constrained approach
Adaptive MBD	Oh model	Fresnel model	Arii's volume model	Nonnegative eigenvalue approach

Freeman MBD using X-Bragg represents for Freeman three-component decomposition using X-Bragg Model; Yamaguchi MBD represents for Yamaguchi three-component decomposition; Hybrid MBD stands for iterative generalized hybrid model-based decomposition whereas Adaptive MBD stands for adaptive model-based decomposition.

scheme also ensures that all the decomposed components have nonnegative powers. The approach is applied to polarimetric SAR data to retrieve soil moisture under vegetation cover in agricultural areas.

For comparison, three existing MBD models for soil moisture inversion are also tested: 1) the modified Freeman–Durden decomposition, where the ground component is replaced with the X-Bragg model [32], referred to as the Freeman MBD using X-Bragg; for this model, the angular-distribution width parameter characterizing the surface roughness was set as $\pi/6$ as in [32]; 2) the replacement of the volume scattering model with a library of three volume models proposed by Yamaguchi *et al.* [39] in the Freeman–Durden decomposition, referred to as Yamaguchi MBD; and 3) an iterative generalized hybrid MBD (referred to as Hybrid MBD) which combines model-based and eigenvalue-based decomposition techniques together with a generalized vegetation model, in which a physically constrained approach is employed to determine the volume scattering intensity [35]. The methods tested in this paper are summarized in Table I.

III. STUDY AREA AND DATA SET

The airborne and ground data used in this paper were collected during the third Soil Moisture Active Passive Experiment (SMAPEx-3), conducted on September 5–23, 2011, in the Yanco study area in southeastern Australia [50]. The aim of the experiment was to collect airborne SAR and passive microwave data for algorithm development for the National Aeronautics and Space Administration Soil Moisture Active Passive mission. The site is a semiarid agricultural area located in the western plains of the Murrumbidgee catchment near the township of Yanco (longitude 146°10′ E, latitude 34°50′ S). Approximately one-third of the area is characterized by intense irrigation activity. The principal crops during the monitoring period were wheat and canola. The study area is flat with elevation changes of only a few meters.

Fully polarimetric L-band (1.26 GHz) data were acquired on nine dates with coincident ground sampling of soil moisture (see Table II). The airborne SAR data acquisition system was the Polarimetric L-band Imaging SAR (PLIS) [51], which is a fully polarimetric L-band SAR sensor and illuminates the ground on either sides of the aircraft at an incidence angle varying from 15° to 50° across the swath. Polarimetric and radiometric calibration of PLIS was accomplished using a distributed forest target in conjunction with six trihedral passive radar calibrators. After calibration, the mean ratio of the copolarized channels

TABLE II
SAR DATA ACQUISITION DATES DURING THE SMAPEX-3 EXPERIMENT. CUMULATIVE PRECIPITATION (THREE DAYS PRIOR TO WHEN THE SMAPEX-3 EXPERIMENT BEGAN) AND PRECIPITATION RECORDED ON THE DAY (BRACKETS) ARE ALSO SHOWN

Date	05/09	07/09	10/09	13/09	
Rain [mm]	0.2 (0.2)	3.6 (3.4)	5.0 (1.6)	5.0 (0)	
	15/09	18/09	19/09	21/09	23/09
	5.0 (0)	5.0 (0)	5.0 (0)	5.0 (0)	5.0 (0)

was 1, and the mean phase difference was 3° and 6° for the left and right antennas, respectively. The absolute and relative calibration accuracies were estimated at 0.9 and 0.8 dB, respectively [50]. After polarimetric and radiometric calibration, the scattering matrix (spatial resolution of approximately 6 and 0.8 m in range and azimuth) was transformed into a coherency matrix (by applying a multilook factor of 2 in range and 14 in azimuth) and projected to ground coordinates at a spatial resolution of 10 m. Speckle noise in the SAR data was reduced using the refined Lee filter with a window size of 7 × 7 [52], which could preserve polarimetric information in homogeneous areas. Additionally, an additive noise suppression filtering algorithm for fully polarimetric data, based on the reduction of the channel correlation $\langle \mathrm{HV} \cdot \mathrm{VH}^* \rangle$, was applied to further reduce additive noise [3].

Soil moisture monitoring was undertaken at about 70 agricultural fields, 39 of which were planted with wheat and canola, while the remaining presented bare conditions. Despite the large number of fields available, most were unsuitable for analysis as they presented stable dry soil moisture conditions throughout the experiment (below 0.2 m^3/m^3). A total of 11 fields were selected for the purpose of this paper which targeted fields with reasonably wide soil moisture dynamic range and a variety of growth stages and crop types (wheat and canola) as observed during the field campaign. Table III lists the main characteristics of the fields used in this analysis, and Fig. 2 displays a polarimetric radar RGB image of the selected fields. Some fields were flood irrigated during the monitoring period (see Table III). A bare soil field was included in the analysis as a control site. Notice that the empirical Oh surface scattering model employed for soil moisture inversion was previously evaluated on 11 bare fields in the same study area and was shown to be the most accurate among three models [53].

TABLE III
CHARACTERISTICS OF SMAPEX-3 AGRICULTURAL FIELDS USED IN THE ANALYSIS

Field #	Crop type	Growth stage	Incidence angle range (°)	Plant height (cm) Week 1/2/3			Nr. Soil moisture sampling	Surface Roughness Root Mean Square [cm]*	Row structure direction	Irrigation date (approx.)
144	Bare	-	15 - 25	-	-	-	2	-	-	-
35	Wheat	Leaf emergence	28 - 35	10	15	31	2	-	-	04/09
4	Wheat	Leaf emergence	23 - 35	16	26	33	4	1.6	-	-
97	Wheat	Stem elongation	37 - 44	35	28	38	3	-	-	10/09
57	Wheat	Stem elongation	29 - 37	41	52	53	4	-	-	-
22	Wheat	Flowering	27 - 34	50	50	50	5	-	N-S	18/09
89	Wheat	Flowering	33 - 45	60	56	50	2	-	E-W	14/09
19	Wheat	Flowering	18 - 29	59	55	64	5	-	-	20/09
17	Wheat	Flowering	34 - 41	65	63	66	7	0.9 (4.6*)	N-S	20/09
29	Wheat	Flowering	37 - 40	54	57	79	2	-	E-W	06/09
96	Canola	Flowering	34 - 42	95	113	118	4	1.0	-	-
95	Canola	Flowering	33 - 42	95	98	140	2	-	-	-

* Large-scale roughness recorded in the direction perpendicular to the row structure
-: Data not available.

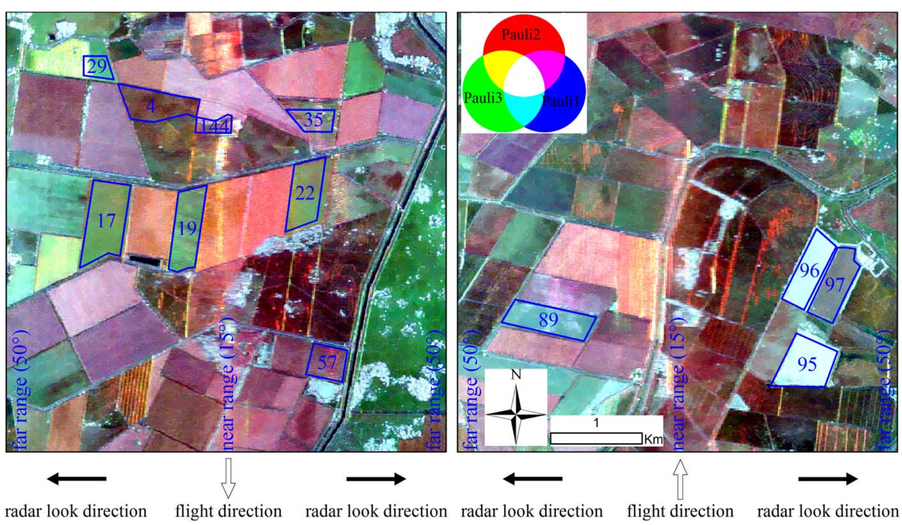

Fig. 2. RGB image of the Pauli decomposition powers (in decibels) of the agricultural study areas using the airborne SAR observations acquired on September 10, 2011; Pauli2 (double-bounce scattering, Red): $|S_{\mathrm{hh}} - S_{\mathrm{vv}}|^2$. Pauli3 (volume scattering, Green): $|S_{\mathrm{hv}}|^2$. Pauli1 (single-bounce scattering, Blue): $|S_{\mathrm{hh}} + S_{\mathrm{vv}}|^2$. The agricultural study area is composed of two parts as shown in the left and right panels. The analyzed agricultural fields are outlined by polygons and labeled with the field number according to Table III.

Although soil moisture was monitored on each of the nine days of airborne SAR acquisition, due to the large number of fields, each field was monitored only once a week, for a total of three visits during the experiment. Soil moisture measurements were conducted using portable dielectric probes over a depth of 0–5 cm on a regular grid of locations equally spaced at 250 m, resulting in 2 to 7 monitoring locations, depending on the field size (see Table III). At each location, three soil moisture replicate measurements were taken within a 1-m radius and averaged to characterize small-scale soil moisture variability. The complex dielectric measurements were converted to volumetric soil moisture (in m^3/m^3) using site-specific calibration equations developed using hundreds of gravimetric samples collected in the area, yielding an estimated accuracy of 0.035 m^3/m^3 [54]. Surface roughness and vegetation characteristics were also measured at 3 of the 12 fields analyzed and are included in Table III. Surface roughness was measured using 3-m-long manual profiles in two directions. Vegetation biomass samples were collected to determine the water content through oven drying. Vegetation conditions varied little during the experiment, with an increase in plant height smaller than 10 cm on average for the wheat and up to 20 cm for the canola. However, the emergence of heads in the flowering wheat was observed during the experiment.

IV. RESULTS AND DISCUSSIONS

The results of four decomposition schemes are analyzed qualitatively in terms of decomposed power components (volume, surface, and double bounce) and vegetation structure parameters. The results for soil moisture estimation are then quantitatively analyzed using ground measurements.

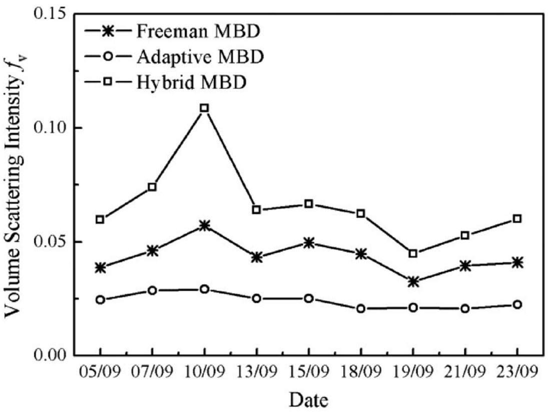

Fig. 3. Time series of the mean volume scattering intensity f_v values over the entire study area by the three different polarimetric decomposition methods. The same volume model (i.e., the random volume model) is employed for the three methods. For the Hybrid MBD, the soil dielectric constant is set as 40 (the maximum possible soil dielectric constant value assumed in vegetated soils), in which the volume scattering intensity will be the smallest.

A. Volume Intensity Estimation

The determination of volume intensity f_v is a critical step for the accurate characterization of the vegetation volume and soil moisture inversion. In the original Freeman MBD, the volume scattering intensity can be directly obtained from the cross-polarization component (i.e., $f_v = 4 \times T_{33}$). The volume scattering intensity is often overestimated since the cross-polarization component is assumed solely from volume scattering [37]. To constrain the volume scattering intensity, a physically constrained solution for the vegetation volume intensity was proposed in the Hybrid MBD [34], [35], in which the contribution of the double-bounce component had to be neglected. Alternatively, a nonnegative eigenvalue approach is utilized in the Adaptive MBD. In order to demonstrate how the three methods vary, the same volume scattering model (i.e., the random volume model) was used for all three methods. Fig. 3 displays the time series of mean volume intensity f_v values over the entire study area obtained from the three approaches described earlier. For the Hybrid MBD, the soil dielectric constant ε_s was set to 40, in which the minimum f_v will be obtained.

It can be seen that the Adaptive MBD has smaller f_v values when compared to the Freeman MBD, indicating a smaller volume component which is consistent with previous observations regarding the overestimation of the volume component by the Freeman MBD [30], [38] and [40]. In contrast, the Hybrid MBD always has much higher f_v values than the Adaptive MBD and the Freeman MBD. This is likely due to the fact that only three terms of the measured coherency matrix (namely, T_{11}, T_{22}, and $|T_{12}|$) are used in the Hybrid MBD and that the scattering from the double-bounce component is neglected when solving for f_v. Overestimated volume intensity f_v leads to nonphysical ground components in the Hybrid MBD due to the negative cross-polarization terms. Since, for our airborne SAR data, most pixels had negative cross-polarization terms in the ground component, the Hybrid MDB method resulted in unsolvable soil moisture inversion over wide areas. It was therefore not further used in this paper. Additional analysis with different SAR data sets is needed to clarify the reasons behind such failure.

B. Comparison of Decomposed Powers

Fig. 4 displays the time series of decomposed powers using the three methods analyzed, namely, the Freeman MBD using X-Bragg, the Yamaguchi MBD, and the Adaptive MBD. The curves indicate the measured vegetation height. For easy display, the comparison is shown for five agricultural fields, namely, fields #4, #97, #17, #29, and #95, chosen to represent the main vegetation types (wheat and canola) and wheat growth stages during the monitoring period (leaf emergence, stem elongation, and flowering; see Table III). Note that all powers are normalized to the total power (i.e., surface + double-bounce + volume), therefore highlighting the relative strength between the three components.

The relative strengths of the decomposition powers reflect changes with vegetation heights and types. In field #4, the wheat was in the stage of leaf emergence, and the height was less than 35 cm (see Table III). In such a case, surface scattering was the dominant scattering mechanism (about 80% of the total power), as expected. Both the double-bounce and volume components were quite low. For wheat in the stem elongation phase (~40-cm height, field #97), the surface component dropped a lot, while the volume component showed a significant increase with respect to field #4. The double-bounce component took up to 10% of the total power. Since the wheat canopy is composed mostly of vertical stalks, the presence of vertical structures in the stage of stem elongation generated a considerable amount of double-bounce scattering. For tall wheat fields (fields #17 and #29), where the wheat plants were of similar height and in the flowering phase and the radar incidence angle was almost the same, the decomposed powers varied. For field #17, the surface component was still dominant, while the double-bounce component indicated an increase with respect to field #97. By contrast, for the tall wheat field #29, the double-bounce component was dominant at most dates. Reasons for this might be associated to the plant row direction (see Table III) as the row direction could shift the phase difference between HH and VV [55]. It is worth mentioning that the emergence of wheat heads may contribute to the volume scattering [56] and alter the ratio between HH and VV polarizations [57], [58]. However, the influence of wheat heads on decomposition results was not obvious in this paper, which requires further investigation with the support of additional ground measurements.

The dominant scattering mechanism changed from surface scattering in wheat fields to mainly volume scattering in the canola fields, with the volume component taking between 50% and 80% of the total power. The plants in field #95 had already grown to a height of about 100 cm when the SMAPEx-3 campaign began. Moreover, the canopy was very dense and lush (4–5-kg/m^2 vegetation water content) relative to the wheat, resulting in the volume scattering dominance observed in Fig. 4. Both the surface and double-bounce components were relatively low.

No significant temporal trends in decomposed volume powers could be associated to plant growth during the monitoring

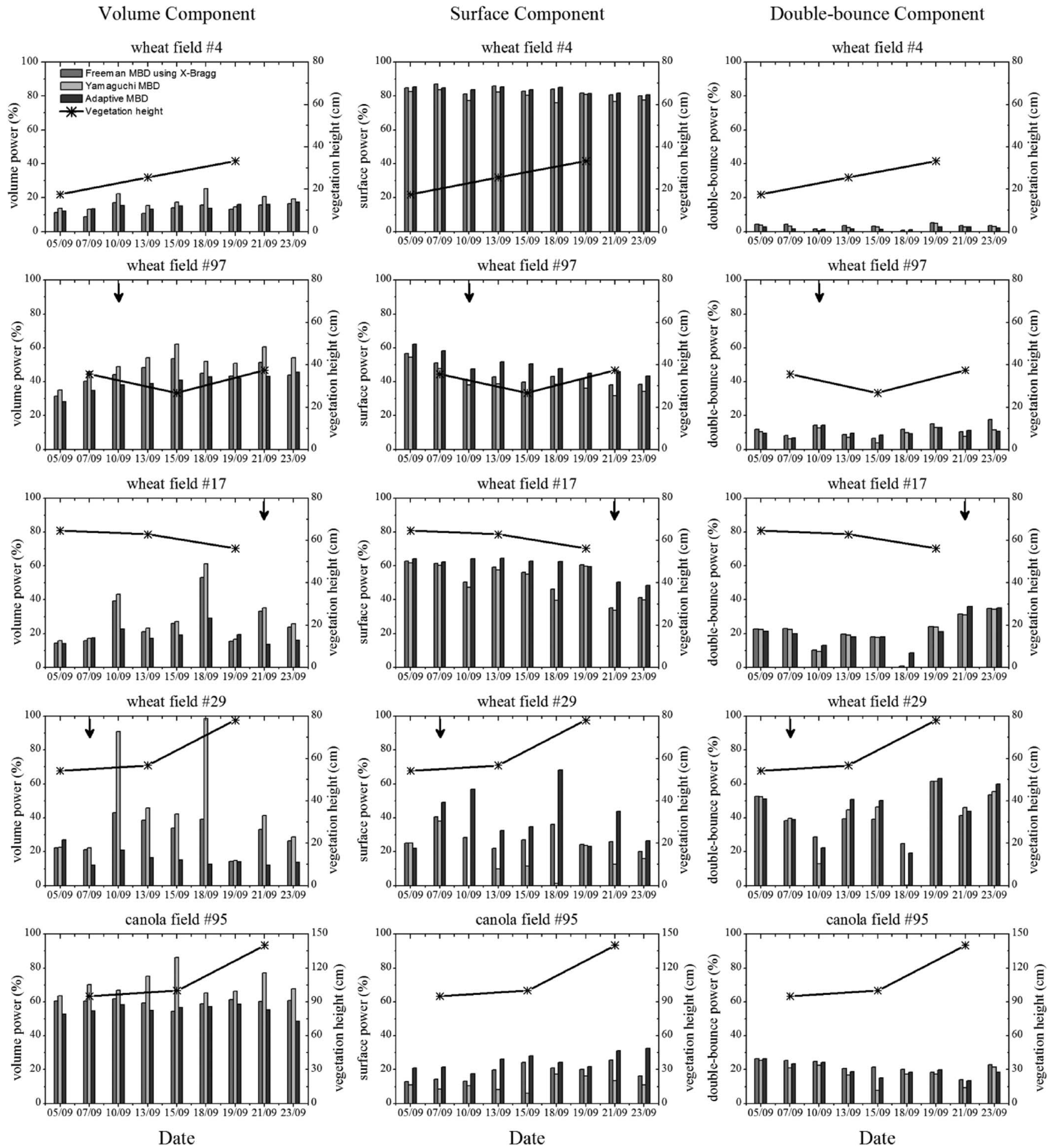

Fig. 4. Time series of relative decomposed powers: (Left column) Volume, (middle column) surface, and (right column) double-bounce scattering for five selected fields with increasing plant heights (top to bottom). The curves show the height of the crop of the respective field. The arrows indicate approximate dates when fields were irrigated.

period except a slight increasing trend in relative volume component observed as the plant height increased in field #97. This was no surprise since, as previously observed, the vegetation conditions varied little during the experiment (see Table III). However, it was surprising that there was no clear correlation between volume component and plant height variability across the four selected wheat fields (fields #4, #97, #17, and #29). It was previously observed that, in the flowering phase, the fresh biomass began to decrease gradually [59], [60]. As a consequence, the wheat became dry and appeared rather transparent at L-band. This may explain why the volume component appeared much stronger in short wheat (field #97) than in tall wheat (fields #17 and #29). These results are in agreement with the findings in [32], suggesting that the volume component

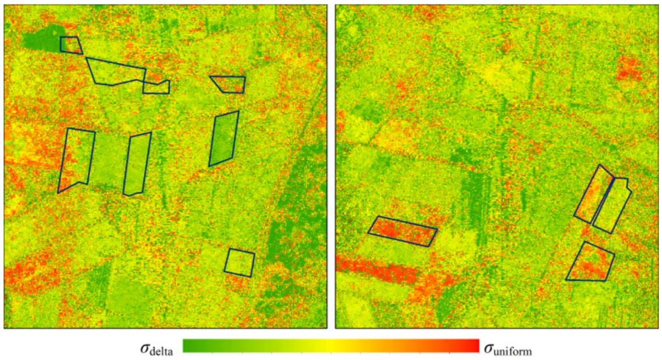

Fig. 5. Randomness maps in the agricultural study areas on September 7, 2011. The analyzed agricultural fields are outlined by the polygons.

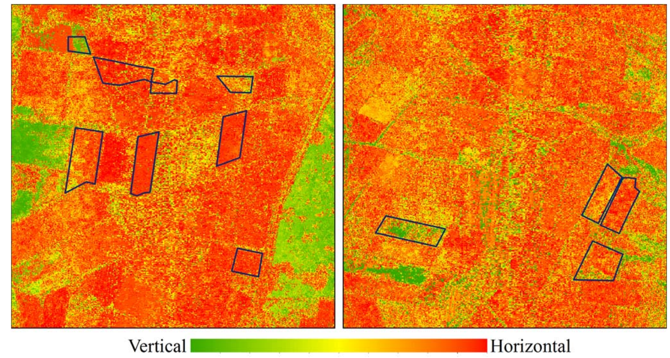

Fig. 6. Mean orientation angle maps in the agricultural study areas on September 7, 2011. The analyzed agricultural fields are outlined by the polygons.

seems to be more sensitive to fresh biomass rather than plant height.

In terms of comparison among different decomposition schemes, the three approaches yielded quite different results. In most fields, particularly tall wheat and canola, the Yamaguchi MBD provided the highest relative volume component, leading to negative surface or double-bounce components for fields #17 and #19 at some dates. Our interpretation of this behavior is that the Yamaguchi MBD assumes that the cross-polarization signal comes solely from the volume scattering. Meanwhile, the volume component fluctuated significantly from day to day, particularly in wheat fields #17 and #29, which was more likely associated to the fluctuations in cross-polarization terms. These problems can be partially solved by introducing the X-Bragg model for slightly rough soil surfaces [32], as shown in the Freeman MBD using X-Bragg. Conversely, the Adaptive MBD resulted in a lower volume component and consequently higher surface or double-bounce components. The Adaptive MBD also provided more temporally stable volume components than both Freeman and Yamaguchi MBDs. Given the short time lag (i.e., from two to three days) between observations and consequent small vegetation changes, the decomposed volume components were not expected to fluctuate significantly. It is worth mentioning that the time lag is not expected to influence the decomposed results and soil moisture retrieval results since the results were obtained separately for each acquisition date. Hence, the stable volume component appears to be an advantage of the Adaptive MBD over the Freeman MBD using X-Bragg and the Yamaguchi MBD.

C. Vegetation Orientation and Randomness Parameters Derived From Adaptive VM

The use of the Adaptive VM allows the estimation of two physical parameters associated to the vegetation structures, namely, the randomness σ and the mean orientation angle θ_0. The randomness map (September 7, 2011) is shown in Fig. 5. A significant difference is observed for the fields selected. Randomness values close to that of the uniform random distribution are found over the canola fields. This is reasonable considering the random structure of canola plants with a larger number of branches variably orientated within the canopy volume. Randomness values close to the delta distribution were found over the wheat fields, with the exceptions of fields #17 and #89. A low randomness value corresponds to the case of a cloud of particles tightly oriented around the mean orientation angle, which agree well with the structure of wheat plants.

The mean orientation angle map (September 7, 2011) is shown in Fig. 6. The spatial distribution of θ_0 reveals that most pixels had horizontal orientations over the agricultural study area. Furthermore, the wheat fields exhibited more horizontal orientations. This result is not surprising. For fields covered with short to medium wheat plants (e.g., fields #4 and #97 in Fig. 4), horizontal orientations more likely result from the expected bending of wheat leaves, as the length of the wheat leaf was comparable to the radar wavelength, which is consistent with the results in [35]. However, over fields of tall wheat plants with vertical stalks (e.g., fields #17 and #29 in Fig. 4), a strong double-bounce scattering emerges which could raise the horizontal contribution due to the Fresnel reflections at the trunk and ground surface, as previously observed in [27]. Therefore, the results presented for the Adaptive VM agree with expectations based on the known plant structure.

D. Soil Moisture Inversion Rate

The rate of successfully inverted pixels was calculated and compared for the various methods analyzed. For each field, the inversion rate was calculated as the amount of pixels in the field that can be successfully inverted relatively to the total SAR pixels covering the field, and then, the cumulated rate was calculated across all dates. Fig. 7 shows the averaged inversion rates for each field. On average, the Adaptive MBD resulted in a much higher inversion rate than the Freeman MBD using X-Bragg and the Yamaguchi MBD (both for surface and double-bounce components), successfully inverting approximately 70% and 20% of pixels (respectively for surface and double-bounce components, depending on the scattering dominance) as opposed to approximately 15% and 10% inverted with the Freeman MBD using X-Bragg. The inversion rates for the Freeman MBD using X-Bragg and the Yamaguchi MBD are consistent with the results in [32] using a different SAR data set. However, the inversion rate for the Adaptive MDB is comparable with the results of the Hybrid MBD [35], while the latter resulted in nonphysical ground components and failed to retrieve soil moisture with our current SAR data. On a field-by-field basis,

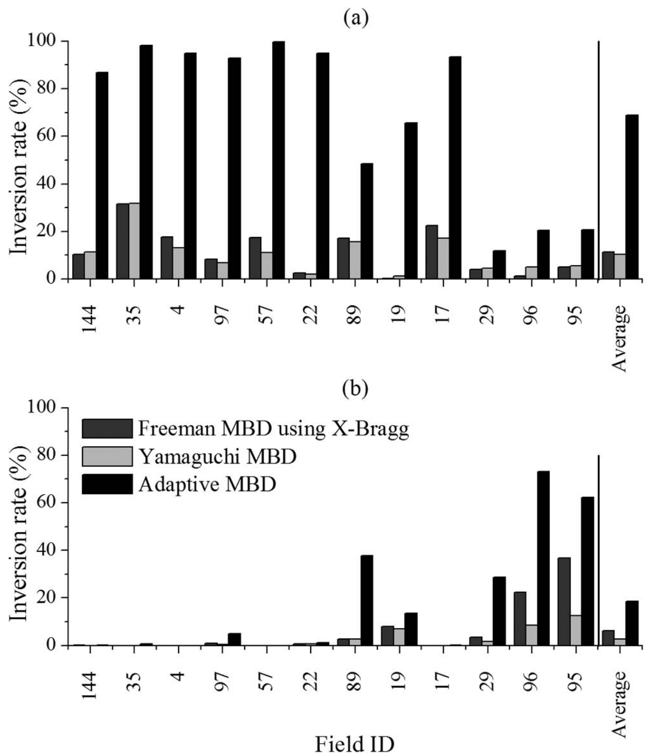

Fig. 7. Successful soil moisture inversion rate (percent of total field pixels) for each field using different decomposition schemes from (a) surface component and (b) double-bounce component. The average inversion rate across all fields is shown on the right-hand side.

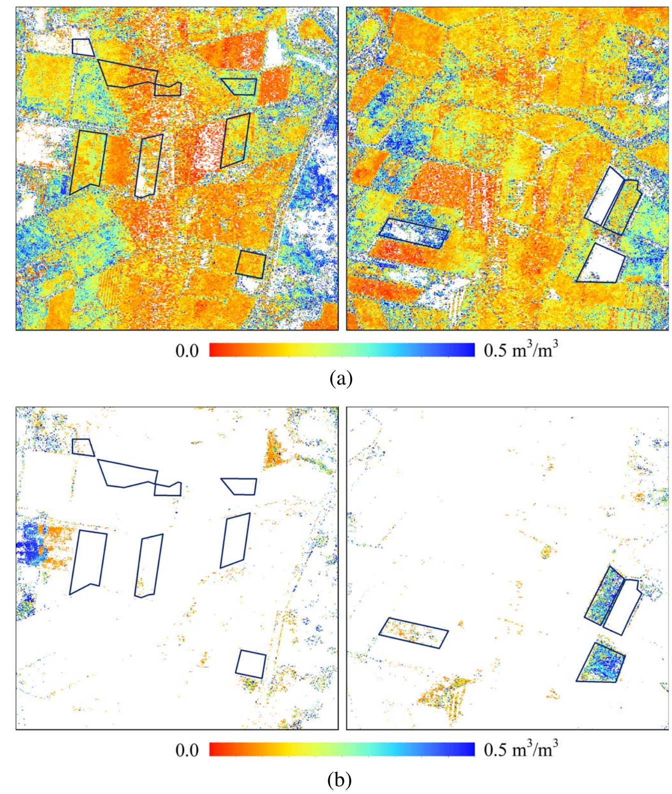

Fig. 8. Soil moisture map obtained from the Adaptive MBD on September 7, 2011 by inverting (a) the surface component and (b) the double-bounce component. Noninvertible pixels appear white.

the Adaptive MBD consistently inverted more pixels than the Freeman MBD using X-Bragg and the Yamaguchi MBD. Such higher inversion rate allows the Adaptive MBD to provide a more comprehensive characterization of the soil moisture spatial distribution with respect to the Freeman MBD using X-Bragg and the Yamaguchi MBD. The inversion rate of the surface component was also higher than that of the double-bounce component for most wheat fields, while for the canola fields, the inversion rate of the double-bounce component was higher.

E. Validation of Soil Moisture Estimation

Fig. 8 shows an example of soil moisture maps (September 7, 2011) obtained from the inversion of the surface and double-bounce components using the Adaptive MBD. Noninvertible pixels appear white. Results from the surface component indicate a higher inversion rate than that of the double-bounce component. However, the inverted pixels from the double-bounce component are complementary to those from the surface component, providing a more complete map of the soil moisture distribution.

The validation of soil moisture estimated from polarimetric decomposition was performed against ground measurements within each field listed in Table III. To avoid errors caused by landscape spatial heterogeneity and also obtain sufficient SAR estimates considering the inversion rate, the SAR estimates were extracted using a window of 21 $\times$ 21 pixels centered around each ground measurement location. For each ground measurement, only the SAR estimates with sufficient percentage (i.e., 30%) of successful retrieval within the 21 $\times$ 21 window were selected. The extracted SAR pixels and ground measurements were then averaged on a field-by-field basis and compared.

Time series of SAR estimates and ground-based soil moisture are presented in Fig. 9 for the three decomposition schemes analyzed. The ground measurements are presented with $\pm$20% interval of their total range instead of standard deviation since, occasionally, there were not enough points per field to calculate the standard deviation. The Adaptive MBD was the only method able to track the soil moisture dynamics in most wheat fields and the gradual dry-down pattern in the canola fields, while the Freeman MBD using X-Bragg and the Yamaguchi MBD could not provide continuous soil moisture estimates for the selected fields. Over a bare soil surface (e.g., field #144) and wheat fields of intermediate height (up to 55 cm, e.g., fields #4, #35, #97, and #57), the Adaptive MBD was able to track changes in soil moisture with some exceptions. For instance, in field #97, the algorithm was able to track the strong increase in soil moisture up to 0.4 m^3/m^3, whereas for field #35, soil moisture was underestimated on September 5. The Adaptive MBD was also able to track soil moisture dynamics on some of the tall wheat fields (#17, #19, and #22) and canola fields (#95 and #96), albeit with underestimation in field #96.

Despite some encouraging results, the performance of the Adaptive MBD was not robust under all conditions. Although, in fields #17 and #19, the ground observations were matched in most cases, the large fluctuations in estimated soil moisture between ground sampling days seem unrealistic since no irrigation or rain was recorded during that period (see Table II). These

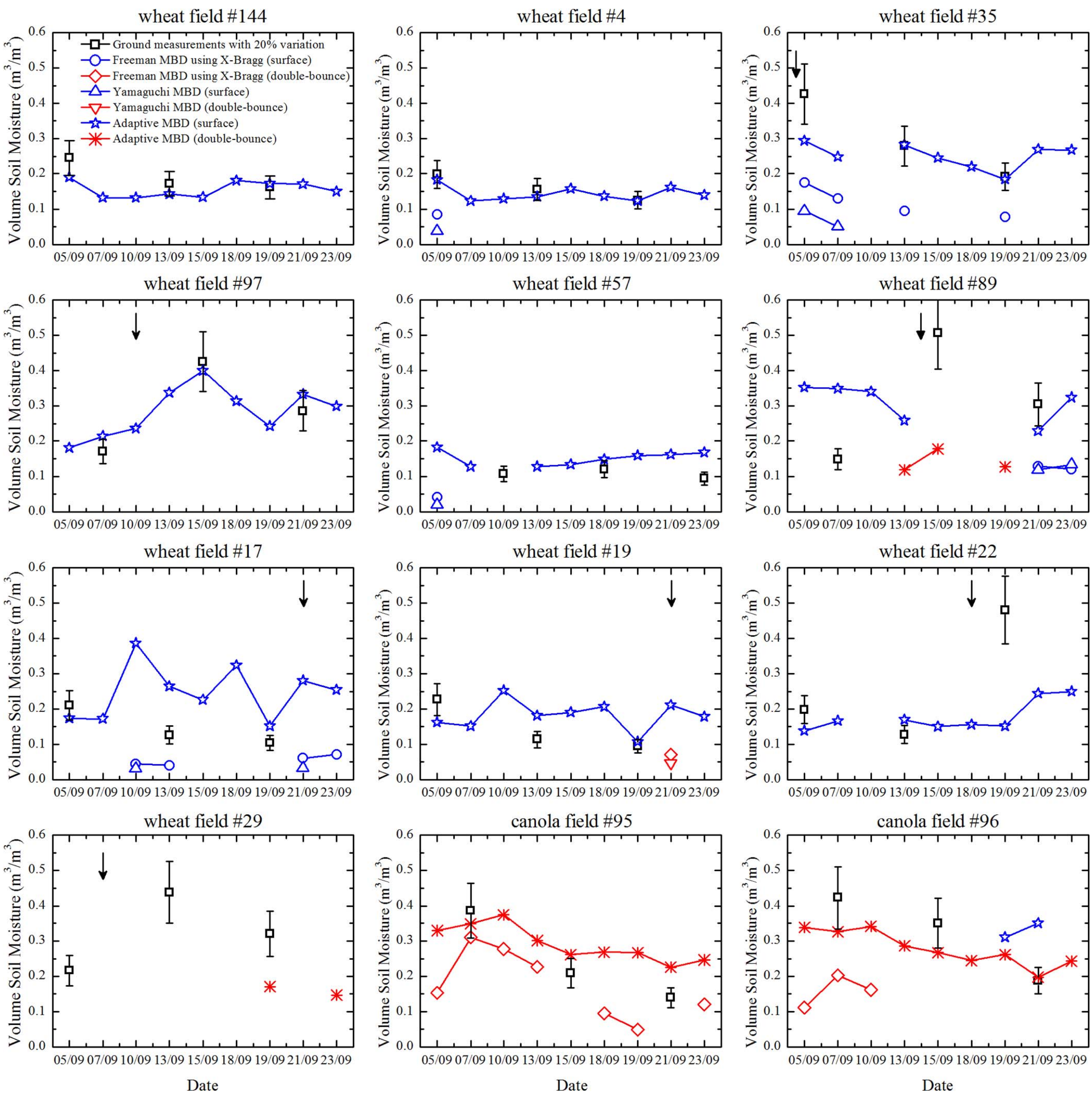

Fig. 9. Time series of field-averaged soil moisture estimated from different polarimetric decomposition methods as compared to ground measurements. The ground measurements are presented with ±20% interval. The arrows indicate approximate dates when fields were irrigated.

fluctuations appeared to be associated with the large fluctuations in the cross-polarization terms observed for fields #17 (see Fig. 4) and #19, rather than a geophysical factor. Moreover, the Adaptive MBD failed to pick up wet soil moisture conditions on days immediately following flood irrigation for certain wheat fields (i.e., field #17 on September 21, field #19 on September 21, and field #22 on September 18) and almost failed to retrieve soil moisture for wheat fields #29 and #89.

To understand the different performances of the three polarimetric decomposition models (namely, the Freeman MBD using X-Bragg, the Yamaguchi MBD, and the Adaptive MBD), the scatterplots of $\mathrm{Re}(T_{12})$ versus $\mathrm{Re}(S_{\mathrm{hh}}S_{\mathrm{vv}}^{*})$ after decomposition using the three models for surface and double-bounce components are shown in Fig. 10. Surface scattering usually has a positive $\mathrm{Re}(S_{\mathrm{hh}}S_{\mathrm{vv}}^{*})$ value, while double-bounce scattering has a negative $\mathrm{Re}(S_{\mathrm{hh}}S_{\mathrm{vv}}^{*})$ value [29], [61], which is consistent with the Bragg model [32] and Fresnel model [32] for surface and double-bounce scattering, respectively. Opposite to the term $\mathrm{Re}(S_{\mathrm{hh}}S_{\mathrm{vv}}^{*})$, a negative $\mathrm{Re}(T_{12})$ value (corresponding to HH $<$ VV) indicates surface scattering, while a positive $\mathrm{Re}(T_{12})$ (corresponding to HH $>$ VV) represents double-bounce scattering. Consequently, positive $\mathrm{Re}(S_{\mathrm{hh}}S_{\mathrm{vv}}^{*})$ and negative $\mathrm{Re}(T_{12})$ would be the physically feasible conditions for surface scattering, while double-bounce scattering

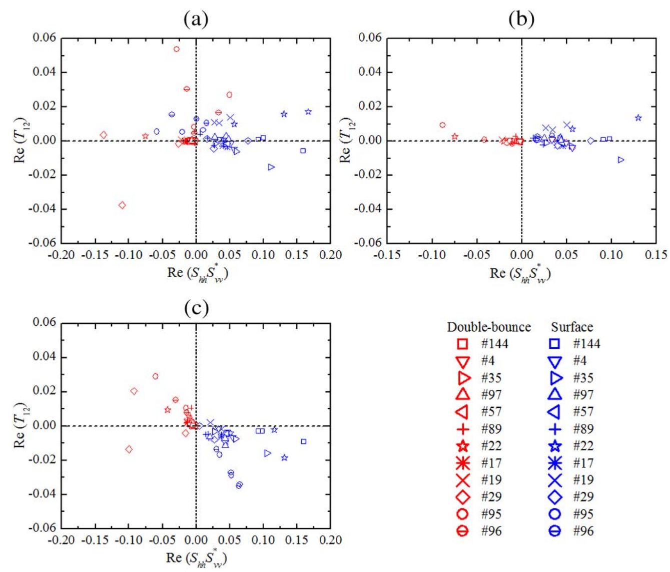

Fig. 10. Scatterplot of $\mathrm{Re}(T_{12})$ versus $\mathrm{Re}(S_{\mathrm{hh}}S_{\mathrm{vv}}^*)$ from the 12 fields analyzed for (a) Freeman MBD using X-Bragg, (b) Yamaguchi MBD, and (c) Adaptive MBD. $\mathrm{Re}(T_{12})$ and $\mathrm{Re}(S_{\mathrm{hh}}S_{\mathrm{vv}}^*)$ values are averaged on a field-by-field basis for the dates when ground soil moisture measurements were available.

has negative $\mathrm{Re}(S_{\mathrm{hh}}S_{\mathrm{vv}}^*)$ and positive $\mathrm{Re}(T_{12})$ values. A pixel outside these regions cannot be inverted. For the Freeman MBD using X-Bragg and the Yamaguchi MBD, most points are outside the physically feasible regions with some exceptions for fields #35, #95, and #96. Therefore, both methods failed to provide continuous and accurate soil moisture estimates. The application of Adaptive MBD could obtain physically meaningful surface or double-bounce components for soil moisture inversion. Fig. 10 can explain well the different performances of the three decomposition approaches. The Adaptive MBD is the only one to obtain physically meaningful surface or double-bounce components for most fields and therefore allow more accurate soil moisture estimation. More physically correct ground components appear to be an advantage of the Adaptive VM over the simple volume scattering models in the Freeman MBD using X-Bragg and the Yamaguchi MBD.

Fig. 10 can also help understanding why the Adaptive MBD failed to obtain soil moisture inversion results for wheat fields #29 and #89. For wheat field #29, pairs of $\mathrm{Re}(S_{\mathrm{hh}}S_{\mathrm{vv}}^*)$ and $\mathrm{Re}(T_{12})$ are outside the valid region, and therefore, inversion for soil moisture failed. For wheat field #89, $\mathrm{Re}(S_{\mathrm{hh}}S_{\mathrm{vv}}^*)$ and $\mathrm{Re}(T_{12})$ values for both surface and double-bounce components were around zero, indicating that the powers of the surface and double-bounce components were close to each other. An erroneous determination of the dominance of surface and double-bounce components can occur, and consequently, the decomposition solution may not be stable. This can also be seen in Fig. 7 (for field #89), where the surface component and double-bounce component have comparable inversion rates. Therefore, the failure of soil moisture inversion over field #89 is most likely related to the instability of the decomposition solution, which may be solved by using an alternative scattering dominance criterion accounting for vegetation conditions (i.e., vegetation type and plant height) [29], [33], [34], [37], [62].

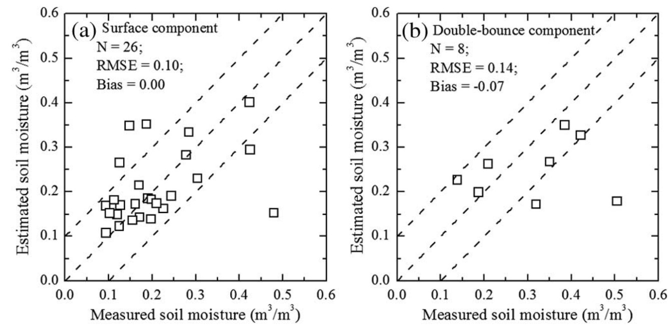

Fig. 11. Comparison of the estimated and the measured soil moisture from the Adaptive MBD for (a) surface component and (b) double-bounce component. N is the number of pairs of points.

It is worth noting (see Table III) that field #97 did not present a row structure, while the remaining fields with tall wheat where soil moisture retrieval was not always successful (fields #22, #89, #17, #19, and #29) presented a row structure. Row structure was associated with the large-scale roughness of the soil surface on the order of tens of centimeters (vertical) and hundreds of centimeters (planimetric) [63]. Since large-scale roughness is known to cause a rotation of the scattering plane, it contributes to depolarization effects and cross-polarization signals. Moreover, with the presence of row structure, the radar look direction (particularly relative to the row direction) will have a significant impact on surface scattering since the backscatter from a field viewed with the look direction perpendicular to the row direction can be much stronger than the look directions off perpendicular [64], [65]. Therefore, the failure of the retrieval scheme in such fields is likely associated with the confounding effect of the row structure.

Soil moisture retrieval results from the Adaptive MBD for the selected 12 fields were quantitatively validated against ground measurements as shown in the scatterplots of Fig. 11. The surface component had 26 pairs of points, while the double-bounce component had 8, which is consistent with the observation of continuity of time-series soil moisture shown in Fig. 9. The Adaptive MBD overall resulted in a root-mean-square error (RMSE) value of 0.10 m^3/m^3 and a bias value of 0.00 m^3/m^3 for the surface component and an RMSE value of 0.14 m^3/m^3 and a bias value of -0.07 m^3/m^3 for the double-bounce component. Although the uncertainty is certainly elevated, the method analyzed in this paper makes exclusive use of the polarimetric information contained in the SAR data, without any *a priori* information on the vegetation structures. The method analyzed also makes the most of the adaptive volume scattering model and the NNED so that it is very appealing for application in agricultural studies and can ensure that the decomposed scattering components are nonnegative.

It should be noted that the proposed decomposition was tested over flat terrain. For more rugged areas, slopes in the azimuth direction could induce polarization orientation angle shifts [66], [67], which could affect the polarimetric radar signatures and, consequently, the polarimetric decomposition results [68], [69]. Furthermore, the presence of azimuth slopes could also lead to incorrect estimates of volume orientation angle in the Adaptive VM [70]. Due to the characteristics of the study area, the impact of orientation angle is assumed to be minimal in this paper. However, the effect of polarization orientation angle has to be taken into account when the proposed decomposition is applied to hilly areas.

It is important to remember that the decomposed ground scattering components (i.e., surface and double-bounce scattering components) are attenuated by extinction through the vegetation canopy [44], [49]. In order to make exclusive use of the polarimetric information contained in the SAR data, the extinction coefficients from different polarizations are assumed to be equal so that the attenuation effects are cancelled out and, consequently, no bias occurs on the soil moisture retrieval for randomly oriented vegetation cover. However, the presence of volume orientation introduces an additional imbalance in extinction coefficients between H and V polarizations and would introduce an estimation error [26], which is not accounted for in this paper. Therefore, soil moisture retrieval accuracy is expected to be improved with information on differential extinction coefficients, which could be retrieved using polarimetric decomposition with *a priori* knowledge of crop height [44] or polarimetric interferometric SAR [71], [72].

V. Conclusion

This paper provided an extensive analysis of soil moisture estimation in agricultural crop fields from fully polarimetric L-band SAR data using an adaptive polarimetric decomposition of the SAR coherency matrix. The adaptive nonnegative decomposition model proposed in [27] was extended into a novel soil moisture retrieval scheme. The proposed Adaptive MBD has been validated using fully polarimetric L-band SAR data acquired in the frame of the SMAPEx-3 campaign over a time span of three weeks in 2011 in southeastern Australia. In addition, soil moisture inversion from the proposed model was compared with previous MBD methods (see Table I).

The results indicated that, among all the decomposition models tested, the Adaptive MBD developed in this paper resulted in lower and more temporarily stable volume scattering components when compared to previous decomposition models. The use of a nonnegative eigenvalue approach proved to be effective in constraining the volume intensity and ensuring the nonnegativity of decomposed scattering powers.

The proposed decomposition incorporates an Adaptive VM [38], which allows for two physical parameters (i.e., the mean orientation angle and the randomness) to be estimated. The results from these two parameters agree with expectations based on the known plant structure, demonstrating the performance of the Adaptive VM in describing volume scattering from vegetation canopy in wheat and canola fields.

The results also demonstrated that a successful retrieval was subject to valid surface or double-bounce scattering components. The proposed Adaptive MBD was superior in achieving physically correct ground components for soil moisture inversion with respect to previous decomposition methods, due to the utilization of an adaptive volume scattering model [38]. This allowed for better soil moisture estimates when compared to other methods. More importantly, it allowed for the retrieval of a more continuous soil moisture time series and a higher inversion rate, thus providing a better spatial characterization of the soil moisture heterogeneity across the agricultural fields. The results also suggest that, depending on the crop type, either surface or double-bounce scattering components are suitable in tracking soil moisture dynamics in agricultural fields. Soil moisture retrieval from the double-bounce component was more efficient in the case of elevated biomass fields (e.g., canola), while the surface scattering was a better option on fields with low and intermediate biomass levels (e.g., wheat).

Finally, the performance of the proposed method was not robust under all conditions. The failures were most likely related to confounding scattering processes due to the presence of row structures in the underlying soil surface. One open question which warrants further analysis is the improvement of the surface scattering model so that it can better describe the complex scattering process with the presence of row structures, which would, in turn, improve the soil moisture inversion accuracy.

Acknowledgment

The authors would like to thank all the third Soil Moisture Active Passive Experiment participants. The authors would also like to thank the reviewers for their very detailed comments that helped improve the quality of this paper.

References

[1] S. R. Cloude and K. P. Papathanassiou, "Surface roughness and polarimetric entropy," in *Proc. IEEE Int. Geosci. Remote Sens. Symp.*, Hamburg, Germany, 1999, pp. 2443–2445.

[2] D. L. Schuler, J.-S. Lee, D. Kasilingam, and G. Nesti, "Surface roughness and slope measurements using polarimetric SAR data," *IEEE Trans. Geosci. Remote Sens.*, vol. 40, no. 3, pp. 687–698, Mar. 2002.

[3] I. Hajnsek, E. Pottier, and S. R. Cloude, "Inversion of surface parameters from polarimetric SAR," *IEEE Trans. Geosci. Remote Sens.*, vol. 41, no. 4, pp. 727–744, Apr. 2003.

[4] S.-E. Park, W. M. Moon, and D.-J. Kim, "Estimation of surface roughness parameter in intertidal mudflat using airborne polarimetric SAR data," *IEEE Trans. Geosci. Remote Sens.*, vol. 47, no. 4, pp. 1022–1031, Apr. 2009.

[5] N. Baghdadi *et al.*, "A potential use for the C-band polarimetric SAR parameters to characterize the soil surface over bare agriculture fields," *IEEE Trans. Geosci. Remote Sens.*, vol. 50, no. 10, pp. 3844–3858, Oct. 2012.

[6] A. Iodice, A. Natale, and D. Riccio, "Retrieval of soil surface parameters via a polarimetric two-scale model," *IEEE Trans. Geosci. Remote Sens.*, vol. 49, no. 7, pp. 2531–2547, Jul. 2011.

[7] A. Iodice, A. Natale, and D. Riccio, "Polarimetric two-scale model for soil moisture retrieval via dual-pol HH-VV SAR data," *IEEE J. Sel. Topics Appl. Earth Observ. Remote Sens.*, vol. 6, no. 3, pp. 1163–1171, Jun. 2013.

[8] P. Ferrazzoli *et al.*, "The potential of multifrequency polarimetric SAR in assessing agricultural and arboreous biomass," *IEEE Trans. Geosci. Remote Sens.*, vol. 35, no. 1, pp. 5–17, Jan. 1997.

[9] F. Mattia *et al.*, "Multitemporal C-band radar measurements on wheat fields," *IEEE Trans. Geosci. Remote Sens.*, vol. 41, no. 7, pp. 1551–1560, Jul. 2003.

[10] X. Blaes *et al.*, "C-band polarimetric indexes for maize monitoring based on a validated radiative transfer model," *IEEE Trans. Geosci. Remote Sens.*, vol. 44, no. 4, pp. 791–800, Apr. 2006.

[11] J. M. Lopez-Sanchez and J. D. Ballester-Berman, "Potentials of polarimetric SAR interferometry for agriculture monitoring," *Radio Sci.*, vol. 44, no. 2, 2009, Art. no. RS2010.

[12] S. Maity, C. Patnaik, J. S. Parihar, S. Panigrahy, and K. A. Reddy, "Study of physical phenomena of vegetation using polarimetric scattering indices and entropy," *IEEE J. Sel. Topics Appl. Earth Observ. Remote Sens.*, vol. 4, no. 2, pp. 432–438, Jun. 2011.

[13] N. Baghdadi *et al.*, "Operational performance of current synthetic aperture radar sensors in mapping soil surface characteristics in agricultural

environments: Application to hydrological and erosion modelling," *Hydrol. Process.*, vol. 22, no. 1, pp. 9–20, 2008.

[14] E. T. Engman and N. Chauhan, "Status of microwave soil moisture measurements with remote sensing," *Remote Sens. Environ.*, vol. 51, no. 1, pp. 189–198, 1995.

[15] M. M. Rahman *et al.*, "Mapping surface roughness and soil moisture using multi-angle radar imagery without ancillary data," *Remote Sens. Environ.*, vol. 112, no. 2, pp. 391–402, 2008.

[16] M. Aubert *et al.*, "Toward an operational bare soil moisture mapping using TerraSAR-X data acquired over agricultural areas," *IEEE J. Sel. Topics Appl. Earth Observ. Remote Sens.*, vol. 6, no. 2, pp. 900–916, Apr. 2013.

[17] R. Bindlish and A. P. Barros, "Parameterization of vegetation backscatter in radar-based, soil moisture estimation," *Remote Sens. Environ.*, vol. 76, no. 1, pp. 130–137, 2001.

[18] A. T. Joseph, R. van der Velde, P. E. O'Neill, R. H. Lang, and T. Gish, "Soil moisture retrieval during a corn growth cycle using L-band (1.6 GHz) radar observations," *IEEE Trans. Geosci. Remote Sens.*, vol. 46, no. 8, pp. 2365–2374, Aug. 2008.

[19] M. A. Karam, A. K. Fung, R. H. Lang, and N. S. Chauhan, "A microwave scattering model for layered vegetation," *IEEE Trans. Geosci. Remote Sens.*, vol. 30, no. 4, pp. 767–784, Jul. 1992.

[20] R. H. Lang and J. S. Sighu, "Electromagnetic backscattering from a layer of vegetation: A discrete approach," *IEEE Trans. Geosci. Remote Sens.*, vol. GE-21, no. 1, pp. 62–71, Jan. 1983.

[21] S.-B. Kim *et al.*, "Soil moisture retrieval using time-series radar observations over bare surfaces," *IEEE Trans. Geosci. Remote Sens.*, vol. 50, no. 5, pp. 1853–1863, May 2012.

[22] A. Balenzano, F. Mattia, G. Satalino, and M. Davidson, "Dense temporal series of C- and L-band SAR data for soil moisture retrieval over agricultural crops," *IEEE J. Sel. Topics Appl. Earth Observ. Remote Sens.*, vol. 4, no. 2, pp. 439–450, Jun. 2011.

[23] N. E. C. Verhoest *et al.*, "A possibilistic approach to soil moisture retrieval from ERS synthetic aperture radar backscattering under soil roughness uncertainty," *Water Resour. Res.*, vol. 43, no. 7, 2007, Art. no. W07435.

[24] C. Notarnicola, M. Angiulli, and F. Posa, "Soil moisture retrieval from remotely sensed data: Neural network approach versus Bayesian method," *IEEE Trans. Geosci. Remote Sens.*, vol. 46, no. 2, pp. 547–557, Feb. 2008.

[25] H. S. Srivastava, P. Patel, M. L. Manchanda, and S. Adiga, "Use of multi-incidence angle RADARSAT-1 SAR data to incorporate the effect of surface roughness in soil moisture estimation," *IEEE Trans. Geosci. Remote Sens.*, vol. 41, no. 7, pp. 1638–1640, Jul. 2003.

[26] T. Jagdhuber, I. Hajnsek, A. Bronstert, and K. P. Papathanassiou, "Soil moisture estimation under low vegetation cover using a multi-angular polarimetric decomposition," *IEEE Trans. Geosci. Remote Sens.*, vol. 51, no. 4, pp. 2201–2215, Apr. 2013.

[27] M. Arii, J. J. van Zyl, and K. Yunjin, "Adaptive model-based decomposition of polarimetric SAR covariance matrices," *IEEE Trans. Geosci. Remote Sens.*, vol. 49, no. 3, pp. 1104–1113, Mar. 2011.

[28] S. R. Cloude and E. Pottier, "An entropy based classification scheme for land applications of polarimetric SAR," *IEEE Trans. Geosci. Remote Sens.*, vol. 35, no. 1, pp. 68–78, Jan. 1997.

[29] A. Freeman and S. L. Durden, "A three-component scattering model for polarimetric SAR data," *IEEE Trans. Geosci. Remote Sens.*, vol. 36, no. 3, pp. 963–973, May 1998.

[30] J. J. van Zyl, M. Arii, and K. Yunjin, "Model-based decomposition of polarimetric SAR covariance matrices constrained for nonnegative eigenvalues," *IEEE Trans. Geosci. Remote Sens.*, vol. 49, no. 9, pp. 3452–3459, Sep. 2011.

[31] H. McNairn and B. Brisco, "The application of C-band polarimetric SAR for agriculture: A review," *Can. J. Remote Sens.*, vol. 30, no. 3, pp. 525–542, 2004.

[32] I. Hajnsek, T. Jagdhuber, H. Schon, and K. P. Papathanassiou, "Potential of estimating soil moisture under vegetation cover by means of PolSAR," *IEEE Trans. Geosci. Remote Sens.*, vol. 47, no. 2, pp. 442–454, Feb. 2009.

[33] M. Arii, "Retrieval of soil moisture under vegetation using polarimetric radar," Ph.D. dissertation, Div. Eng. Appl. Sci., California Inst. Technol., Pasadena, CA, USA, 2009.

[34] T. Jagdhuber, "Soil parameter retrieval under vegetation cover using SAR polarimetry," Ph.D. dissertation, Faculty Sci., Univ. Potsdam, Potsdam, Germany, 2012.

[35] T. Jagdhuber, I. Hajnsek, and K. P. Papathanassiou, "An iterative generalized hybrid decomposition for soil moisture retrieval under vegetation cover using fully polarimetric SAR," *IEEE J. Sel. Topics Appl. Earth Observ. Remote Sens.*, vol. 8, no. 8, pp. 3911–3922, Aug. 2015.

[36] J. J. Van Zyl, K. Yunjin, and M. Arii, "Requirements for model-based polarimetric decompositions," in *Proc. IEEE Int. Geosci. Remote Sens. Symp.*, Boston, MA, USA, 2008, pp. 417–420.

[37] S. R. Cloude, *Polarisation: Applications in Remote Sensing*. Oxford, U.K.: Oxford Univ. Press, 2009.

[38] M. Arii, J. J. van Zyl, and K. Yunjin, "A general characterization for polarimetric scattering from vegetation canopies," *IEEE Trans. Geosci. Remote Sens.*, vol. 48, no. 9, pp. 3349–3357, Sep. 2010.

[39] Y. Yamaguchi, T. Moriyama, M. Ishido, and H. Yamada, "Four-component scattering model for polarimetric SAR image decomposition," *IEEE Trans. Geosci. Remote Sens.*, vol. 43, no. 8, pp. 1699–1706, 2005.

[40] Y. Cui *et al.*, "On complete model-based decomposition of polarimetric SAR coherency matrix data," *IEEE Trans. Geosci. Remote Sens.*, vol. 52, no. 4, pp. 1991–2001, Apr. 2014.

[41] J. J. van Zyl, "Application of Cloude's target decomposition theorem to polarimetric imaging radar data," in *Proc. SPIE*, San Diego, CA, USA, 1993, pp. 184–191.

[42] G. Singh, Y. Yamaguchi, S. E. Park, Y. Cui, and H. Kobayashi, "Hybrid Freeman/eigenvalue decomposition method with extended volume scattering model," *IEEE Geosci. Remote Sens. Lett.*, vol. 10, no. 1, pp. 81–85, Jan. 2013.

[43] S. V. Nghiem, S. H. Yueh, R. Kwok, and F. K. Li, "Symmetry properties in polarimetric remote sensing," *Radio Sci.*, vol. 27, no. 5, pp. 693–711, Sep./Oct. 1992.

[44] A. Freeman, "Fitting a two-component scattering model to polarimetric SAR data from forests," *IEEE Trans. Geosci. Remote Sens.*, vol. 45, no. 8, pp. 2583–2592, Aug. 2007.

[45] S. O. Rice, "Reflection of electromagnetic waves from slightly rough surfaces," *Commun. Pure Appl. Math.*, vol. 4, no. 2/3, pp. 351–378, 1951.

[46] A. Iodice, A. Natale, and D. Riccio, "Soil moisture retrieval in moderately vegetated areas via a polarimetric two-scale model," in *Proc. IEEE Int. Geosci. Remote Sens. Symp.*, Melbourne, Vic., Australia, 2013, pp. 759–762.

[47] A. K. Fung, Z. Li, and K. S. Chen, "Backscattering from a randomly rough dielectric surface," *IEEE Trans. Geosci. Remote Sens.*, vol. 30, no. 2, pp. 356–369, Mar. 1992.

[48] Y. Oh, K. Sarabandi, and F. T. Ulaby, "An empirical model and an inversion technique for radar scattering from bare soil surfaces," *IEEE Trans. Geosci. Remote Sens.*, vol. 30, no. 2, pp. 370–381, Mar. 1992.

[49] M. Arii, J. J. van Zyl, and K. Yunjin, "Retrieval of soil moisture under vegetation using polarimetric scattering cubes," in *Proc. IEEE Int. Geosci. Remote Sens. Symp.*, 2010, pp. 1323–1326.

[50] R. Panciera *et al.*, "The Soil Moisture Active Passive Experiments (SMAPEx): Toward soil moisture retrieval from the SMAP mission," *IEEE Trans. Geosci. Remote Sens.*, vol. 52, no. 1, pp. 490–507, Jan. 2014.

[51] D. Gray *et al.*, "PLIS: An airborne polarimetric L-band interferometric synthetic aperture radar," in *Proc. IEEE APSAR*, Seoul, Korea, 2011, pp. 1–4.

[52] J.-S. Lee, M. R. Grunes, and G. De Grandi, "Polarimetric SAR speckle filtering and its implication for classification," *IEEE Trans. Geosci. Remote Sens.*, vol. 37, no. 5, pp. 2363–2373, Sep. 1999.

[53] R. Panciera, M. A. Tanase, K. Lowell, and J. P. Walker, "Evaluation of IEM, Dubois, and Oh radar backscatter models using airborne L-band SAR," *IEEE Trans. Geosci. Remote Sens.*, vol. 52, no. 8, pp. 4966–4979, Aug. 2014.

[54] O. Merlin *et al.*, "Soil moisture measurement in heterogeneous terrain," in *Proc. Int. Congr. MODSIM*, Christchurch, New Zealand, 2007, pp. 2604–2610.

[55] W. F. Silva, B. F. T. Rudorff, A. R. Formaggio, W. R. Paradella, and J. C. Mura, "Discrimination of agricultural crops in a tropical semi-arid region of Brazil based on L-band polarimetric airborne SAR data," *ISPRS J. Photogramm. Remote Sens.*, vol. 64, no. 5, pp. 458–463, 2009.

[56] J. M. Stiles, K. Sarabandi, and F. T. Ulaby, "Electromagnetic scattering from grassland. II. Measurement and modeling results," *IEEE Trans. Geosci. Remote Sens.*, vol. 38, no. 1, pp. 349–356, Jan. 2000.

[57] H. Skriver, M. T. Svendsen, and A. G. Thomsen, "Multitemporal C- and L-band polarimetric signatures of crops," *IEEE Trans. Geosci. Remote Sens.*, vol. 37, no. 5, pp. 2413–2429, Sep. 1999.

[58] M. S. Moran *et al.*, "A RADARSAT-2 quad-polarized time series for monitoring crop and soil conditions in Barrax, Spain," *IEEE Trans. Geosci. Remote Sens.*, vol. 50, no. 4, pp. 1057–1070, Apr. 2012.

[59] A. M. Smith *et al.*, "Multipolarized radar for delineating within-field variability in corn and wheat," *Can. J. Remote Sens.*, vol. 32, no. 4, pp. 300–313, 2006.

[60] M. Jia, L. Tong, Y. Zhang, and Y. Chen, "Multitemporal radar backscattering measurement of wheat fields using multifrequency (L, S, C, and X) and full-polarization," *Radio Sci.*, vol. 48, no. 5, pp. 471–481, 2013.

[61] J. J. Van Zyl, "Unsupervised classification of scattering behavior using radar polarimetry data," *IEEE Trans. Geosci. Remote Sens.*, vol. 27, no. 1, pp. 36–45, Jan. 1989.

[62] T. Jagdhuber, I. Hajnsek, S. Sauer, K. P. Papathanassiou, and A. Bronstert, "Soil moisture retrieval under forest using polarimetric decomposition techniques at P-band," in *Proc. IEEE 9th EUSAR*, 2012, pp. 709–712.

[63] A. Beaudoin, T. Le Toan, and Q. H. J. Gwyn, "SAR observations and modeling of the C-band backscatter variability due to multiscale geometry and soil moisture," *IEEE Trans. Geosci. Remote Sens.*, vol. 28, no. 5, pp. 886–895, Sep. 1990.

[64] M. Zribi, O. Taconet, V. Ciarletti, and D. Vidal-Madjar, "Effect of row structures on radar microwave measurements over soil surface," *Int. J. Remote Sens.*, vol. 23, no. 24, pp. 5211–5224, 2002.

[65] U. Wegmüller *et al.*, "Progress in the understanding of narrow directional microwave scattering of agricultural fields," *Remote Sens. Environ.*, vol. 115, no. 10, pp. 2423–2433, 2011.

[66] J.-S. Lee, D. L. Schuler, and T. L. Ainsworth, "Polarimetric SAR data compensation for terrain azimuth slope variation," *IEEE Trans. Geosci. Remote Sens.*, vol. 38, no. 5, pp. 2153–2163, Sep. 2000.

[67] J.-S. Lee *et al.*, "On the estimation of radar polarization orientation shifts induced by terrain slopes," *IEEE Trans. Geosci. Remote Sens.*, vol. 40, no. 1, pp. 30–41, Jan. 2002.

[68] W. An, C. Xie, X. Yuan, Y. Cui, and J. Yang, "Four-component decomposition of polarimetric SAR images with deorientation," *IEEE Geosci. Remote Sens. Lett.*, vol. 8, no. 6, pp. 1090–1094, Nov. 2011.

[69] J.-S. Lee and T. L. Ainsworth, "The effect of orientation angle compensation on coherency matrix and polarimetric target decompositions," *IEEE Trans. Geosci. Remote Sens.*, vol. 49, no. 1, pp. 53–64, Jan. 2011.

[70] M. Arii, J. van Zyl, and K. Yunjin, "Improvement of adaptive-model based decomposition with polarization orientation compensation," in *Proc. IEEE Int. Geosci. Remote Sens. Symp.*, 2012, pp. 95–98.

[71] I. Hajnsek and S. R. Cloude, "Differential extinction estimation over agricultural vegetation from Pol-InSAR," in *Proc. PolInSAR Workshop*, Frascati, Italy, 2005, pp. 1–29.

[72] M. Neumann, L. Ferro-Famil, and A. Reigber, "Estimation of forest structure, ground, and canopy layer characteristics from multibaseline polarimetric interferometric SAR data," *IEEE Trans. Geosci. Remote Sens.*, vol. 48, no. 3, pp. 1086–1104, Mar. 2010.

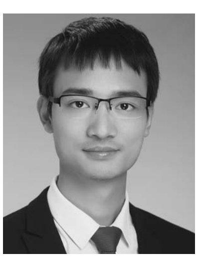

Lian He received the B.S. degree in remote sensing science and technology from Wuhan University, Wuhan, China, in 2010 and is currently working toward the Ph.D. degree in the School of Earth and Space Science, Peking University, Beijing, China.

Between 2013 and 2014, he was with the Department of Civil Engineering, Monash University, Melbourne, Australia, as a Visiting Research Student. His current fields of interest include microwave remote sensing and soil moisture retrieval.

Rocco Panciera (M'12) received the M.S. degree in environmental engineering from the University of Trento, Trento, Italy, in 2003 and the Ph.D. degree in environmental engineering from the University of Melbourne, Melbourne, Australia, in 2009.

He was a Research Fellow with the University of Melbourne between 2009 and 2010, leading a series of large-scale field experiments in southeastern Australia for algorithm development of the National Aeronautics and Space Administration (NASA) Soil Moisture Active Passive mission. From 2011 to 2014, he held the Australian Research Council Super Science Postdoctoral Fellowship at the Cooperative Research Centre for Spatial Information, Melbourne. In this role, he worked on high-resolution estimation of soil moisture and vegetation biomass by airborne and satellite synthetic aperture radar measurements. He currently resides in Bangladesh, where he is involved in a number of development projects related to social geospatial analysis with international NGOs, the United Nations Development Program, and private sector companies. His expertise spans environmental remote sensing, data analytics, and social geographic information systems.

Mihai A. Tanase (M'12) received the engineering diploma in forestry from Stefan cel Mare University, Suceava, Romania, in 1999, the M.Sc. degree in environmental management from the International Centre for Advanced Mediterranean Agronomic Studies, Paris, France, in 2007, and the Ph.D. degree in geography from the University of Zaragoza, Zaragoza, Spain, in 2010.

Between 2011 and 2015, he held a postdoctoral position at the University of Melbourne, Melbourne, Australia, through the ARC Super Science Fellowship program. He is currently a Juan de la Cierva Fellow at the University of Alcala, Alcalá de Henares, Spain. He is a Principal Investigator for ESA ERS, DLR TerraSAR-X, and ALOS-2 projects and participated in the K&C Initiative. His activity is focused on synthetic aperture radar (SAR), InSAR, and PolSAR data for fire severity estimation, vegetation recovery monitoring, and the retrieval of biogeophysical parameters of forests.

Dr. Tanase was the recipient of the IEEE GRSS IGARSS Symposium Interactive Prize Paper Award in 2010.

Jeffrey P. Walker (M'12) received the B.E. (Civil) and B.Surveying degrees with Hons 1 and University Medal from the University of Newcastle, Newcastle, Australia, in 1995 and the Ph.D. degree in water resources engineering from the same university in 1999. His Ph.D. thesis was among the early pioneering research on estimation of root-zone soil moisture from the assimilation of remotely sensed surface soil moisture observations.

He then joined the National Aeronautics and Space Administration (NASA) Goddard Space Flight Center to implement his soil moisture work globally. In 2001, he moved to the Department of Civil and Environmental Engineering, University of Melbourne, Melbourne, Australia, as a Lecturer, where he continued his soil moisture work, including the development of the only Australian airborne capability for simulating new satellite missions for soil moisture. In 2010, he was appointed as Professor in the Department of Civil Engineering at Monash University, Melbourne, Australia, where he is continuing this research. He is contributing to soil moisture satellite missions at NASA, ESA, and JAXA, as a Science Team member for the Soil Moisture Active Passive mission and Cal/val Team member for the Soil Moisture and Ocean Salinity and Global Change Observation Mission-Water, respectively.

Qiming Qin received the B.S. degree in geography from Nanjing Normal University, Nanjing, China, in 1982, the M.S degree in geophysics from Shaanxi Normal University, Xi'an, China, in 1987, and the Ph.D. degree in geophysics from Peking University, Beijing, China, in 1990.

He is currently a Professor with the School of Earth and Space Sciences, Peking University. He also serves as the Secretary General of the National Steering Committee for Geography Education in Universities and Colleges, China, and the Remote Sensing Application Consortium of Universities and Colleges, China.

Dr. Qin is the Executive Director of the Environmental Remote Sensing Commission of the Geographical Society of China and the Director of the China Association for Geographic Information System, the Chinese Society for Geodesy, Photogrammetry and Cartography, the China Hi-Tech Industrialization Association, and the Chinese Association of Young Scientists and Technicians. He has served as an Evaluator of the Domestic GIS software evaluation expert team of the China Association for Geographic Information System in 1996 and a Lead Evaluator of the GIS software Evaluation Committee of the Ministry of Science and Technology of China in 1995.